Chemical Engineering Journal 449 (2022) 137846

Contents lists available at ScienceDirect

Chemical Engineering Journal

journal homepage: www.elsevier.com/locate/cej

Deep NIR-II optical imaging combined with minimally invasive interventional photothermal therapy for orthotopic bladder cancer

Fengqiu Hong [a], Xiaorui Geng [b], Guangzong Min [c], Xiang Sun [a], Bei Zhang [a,d], Youliang Yao [a], Ronghui Li [e], Jing Wang [f], Hengyu Zhao [f], Peng Guo [g], Zhen Yuan [b,*], Xiaofei Wen [h,i,*], Liming Nie [j,*], Gang Liu [a], Xiaoyuan Chen [k,l,m], Qingliang Zhao [a,d,*]

[a] State Key Laboratory of Molecular Vaccinology and Molecular Diagnostics, Center for Molecular Imaging and Translational Medicine, Department of Laboratory Medicine, School of Public Health, Xiamen University, Xiamen 361102, China
[b] Cancer Center, Faculty of Health Sciences, Centre for Cognitive and Brain Sciences, University of Macau, Taipa, Macau Special Administrative Region 999078, China
[c] College of Materials, Xiamen University, 422 Siming Nan Road, Xiamen 361005, China
[d] Shenzhen Research Institute of Xiamen University, Shenzhen 518063, China
[e] Department of Medical Oncology, Xiang'an Hospital of Xiamen University, 2000 East Xiang'an Rd., Xiang'an, Xiamen 361102, China
[f] Department of Radiology, Xiamen Cardiovascular Hospital of Xiamen University, School of Medcine, Xiamen University, Xiamen 361102, China
[g] Capital Institute of Pediatrics, Beijing 100020, China
[h] Department of Interventional Radiology, The First Affiliated Hospital of Xiamen University, Xiamen, Fujian 361000, China
[i] Department of Interventional Radiology, Molecular Imaging Research Center (MIRC), The 4th Hospital of Harbin Medical University, Harbin, Heilongjiang 150001, China
[j] Medical Research Center, Guangdong Provincial People's Hospital, Guangdong Academy of Medical Sciences, Guangzhou 510080, China
[k] Departments of Diagnostic Radiology, Surgery, Chemical and Biomolecular Engineering, and Biomedical Engineering, Yong Loo Lin School of Medicine and Faculty of Engineering, National University of Singapore, Singapore 119074, Singapore
[l] Clinical Imaging Research Centre, Centre for Translational Medicine, Yong Loo Lin School of Medicine, National University of Singapore, Singapore 117599, Singapore
[m] Nanomedicine Translational Research Program, NUS Center for Nanomedicine, Yong Loo Lin School of Medicine, National University of Singapore, Singapore 117597, Singapore

ARTICLE INFO

Keywords:
NIR-II PA/OCTA
Minimally invasive interventional PTT
Laparoscopy and US imaging

ABSTRACT

Surgical resection (SR) is the major method for treating invasive or recurrent noninvasive bladder cancer (BC). However, SR still causes additional risks of urinary tract infection, bleeding and some complications that may be life-threatening. Therefore, it is of urgent medical need for new diagnosis and therapy scheme for BC. Herein, we proposed a strategy that combines dual-modality three-dimensional (3D) NIR-II photoacoustic (PA) and optical coherence tomography angiography (OCTA) molecular imaging to guide visually interventional photothermal therapy (PTT) for BC. Additionally, we developed an excellent NIR-II hyaluronic acid-IR-1048 with liposome-coated (HAPO-1048) photothermal agent for PTT of CD44 overexpressing orthotopic BC, which showed strong NIR-II optical absorption, preferable tumor targeting, excellent biocompatibility and high PTT efficacy. Combined with the NIR-II PA/PTT response of the HAPO-1048, we can achieve high sensitivity and specificity (about 2 mm diameter) dynamic monitoring and investigate the precision therapy of PTT in deep orthotopic BC (4.38 mm). Simultaneously, we can map the dynamic changes of 3D PA signals and HAPO-1048 nanoparticles (HAPO-1048 NPs) enrichment, which is closely related to the PTT efficacy. Significantly, the whole changes of complex microvascular morphometrics and angiogenesis of BC were well surveilled and assessed *in vivo* using OCTA. Lastly, minimally invasive interventional PTT strategy was successfully implemented to achieve a controllable and precise therapy for orthotopic BC based on laparoscopy and US guidance. In conclusion, we present a multimodal NIR-II optical imaging synergy laparoscopy interventional oncologic scheme, which should expand the current PTT technology, leading to a significant ongoing in treatment of primary tumors of urinary system.

* Corresponding authors at: Department of Interventional Radiology, The First Affiliated Hospital of Xiamen University, Xiamen, Fujian 361000, China (X. Wen); State Key Laboratory of Molecular Vaccinology and Molecular Diagnostics, Center for Molecular Imaging and Translational Medicine, Department of Laboratory Medicine, School of Public Health, Xiamen University, Xiamen 361102, China (Q. Zhao).
E-mail addresses: zhenyuan@um.edu.mo (Z. Yuan), Xiaofei5132004@163.com (X. Wen), nieliming@gdph.org.cn (L. Nie), zhaoql@xmu.edu.cn (Q. Zhao).

https://doi.org/10.1016/j.cej.2022.137846
Received 4 May 2022; Received in revised form 19 June 2022; Accepted 27 June 2022
Available online 30 June 2022

1. Introduction

Bladder cancer (BC) is the 6th most commonly diagnosed cancer and the 9th leading cause of cancer deaths for men, with an estimated 570,000 new cases diagnosed each year [1]. As of the initial diagnosis of BC, approximately 75% of patients present with a non-muscle-invasive BC (NMIBC) that is confined to the mucosa (stage Ta or CIS) or submucosa (stage T1). For younger patients (<40 years old) this percentage is even higher [2,3]. Since the development of transurethral resection of bladder tumor (TURBT) and endoscopy as initial diagnostic and staging techniques more than 30 years, there have been no major advances in the diagnosis of BC [4]. Modern endoscopy, white light cystoscopy (WLC) and WLC-assisted TURBT, have resulted in incorrect clinical decisions, missed optimal treatment time, and increased risk of failure due to the inability to recognize and remove some ultra-small tumors or carcinoma in situ (CIS) [5,6]. It is therefore essential to establish a technical approach that can detect BC with high resolution at an early stage.

Currently, advanced optical imaging techniques, such as narrow band imaging (NBI) and digital contrast enhancement has been developed for identifying of CIS. Compared to WLC, they can better visualize surface structures and blood vessels of bladder than WLC [7,8]. However, these imaging modalities also have shortcomings and limitations, such as the lack of specificity, easy misdiagnosis of inflammation, and significant local side effects [9].

Photoacoustic imaging (PAI) is an emerging noninvasive and real-time technology that provides a strong optical contrast and high ultrasonic spatial resolution of photothermal agents in deep scattering media [10]. By detecting optical absorption signals, PAI can provide endogenous structure and functional information of tissues (e.g. lipids, melanin, hemoglobin (Hb) and oxyhemoglobin (HbO_2), blood oxygen saturation (SaO_2), hemoglobin content (HbT)) and exogenous contrast agents signals (e.g. dyes) [10–13]. In particular, at the wavelength (1000–1200 nm) of second near-infrared (NIR-II) PAI has grown interest in recent years because of the improved depth of tissue penetration and having a higher signal-to-background ratio (SBR) compared with PAI in the traditional visible and NIR-I region (700–900 nm) [14–17]. The previous study observed BC by measuring oxygenation of PAI [18], and NIR-II PAI was measured in deep tissues of rat bladders by applying exogenous agents [19]. With its high sensitivity, PAI can be used as an auxiliary method to detect tiny tumors, monitor of oxygenation dynamics, and obtain a deeper image of BC. Furthermore, an emerging optical coherence tomography angiography (OCTA) technology has the ability to detect change of microvascular hemodynamics as well as to provide an ultra-high-resolution image of the tumor structure. With multiple B-scans obtained in the same location, OCTA can provide the three-dimensional (3D) information about depth resolved micro-vessels using endogenous hemoglobin motion contrast [20]. Several preclinical and clinical studies have demonstrated its potential for the diagnosis of BC [21,22]. In this study our integrated NIR-II PA and OCTA is expected to provide a better understanding of the vascular network and neovascularization of BC with high resolution and high image contrast, enabling 3D angiography of structural, functional, and molecular information [23]. Very few reports have combined and maximized the application of these two techniques in BC molecular imaging (MI), or with dynamic visualization and evaluation of the photothermal therapy (PTT) interventional therapeutic process *in vivo*.

Besides the tumor MI, the photothermal effect can generate thermal energy to ablate tumor tissues with precision, controllability and less trauma [24]. Compared with photodynamic therapy (PDT), PTT relies on the irradiation-responsive heat generated from photothermal agents for tumor ablation, which is oxygen-independent. Therefore, PTT is highly effective to ablate solid tumors through design of photothermal agents with high photothermal conversion efficiency. [25]. In previous studies, owing to the limitation of tissue penetration depth of NIR laser light and attenuated efficacy by threshold laser power for skin tolerance, PTT most were used to treat superficial tumor or tumors that are directly exposed to optical fiber through surgical incision [26–29]. To our knowledge, there are still relatively few studies about minimally-invasive PTT with multimodality imaging for early diagnosis and effective ablation of orthotropic BC.

Herein, to replicate the biology of human BC in natural growth and progression, we first constructed the orthotopic BC model through urethra by ultrasound-guided transurethral strategy. In addition, we developed a multifunctional theranostic agent, hyaluronic acid (HA)-modified and liposome-coated IR1048 (HAPO-1048 NPs) for NIR-II PA imaging of BC, which presents strong optical absorbance in the NIR-II region and highly efficient tumor accumulation due to the enhanced permeability and retention (EPR) effect and HA-mediated active targeting to CD44-overexpressing tumor cells in BC. Experimental results showed that HAPO-1048 had excellent NIR-II photostability and PTT effect. Moreover, combined with NIR-II PAI and OCTA, it not only provides deeper insights on microcirculation information, but also has remarkable potential to image deep orthotopic BC and detect small tumors. Significantly, we developed a minimally invasive intervention-guided PTT platform comprised of a laparoscope to intuitively provide the general condition outside the bladder and ultrasound to provide the images of bladder cavity, which exhibits the outstanding ability to monitor the treatment efficacy. It is foreseeable that these technologies have great potential for the precise management and intervention of clinical BC as shown in scheme 1.

2. Results and discussion

2.1. Preparation and Characterization of HAPO-1048 NPs

Nanotheranostics based on exogenous contrast agents has been widely utilized by integrating diagnosis and treatment in a single nanoplatform [30,31]. According to previous research, the platelet membrane protein-loaded materials (BLIPO-1048) had excellent capability of NIR-II PAI and PTT, and could actively target CD44 [32]. Hyaluronic acid (HA), as a widely used biocompatible material [33–36], can also actively target to CD44-overexpressing BC. Compared with BLIPO-1048, the preparation of HA-loaded materials is simpler, and also can be timely and effectively produced and used without considering whether the source of HA needs to be from the same individual or race. Hence, we synthesized and utilized HAPO-1048 by a thin film hydration method (Fig. 1a). According to the complete disruption and fusion of the liposomes during the thaw process -after extrusion, the HA was equally dispersed between the intraliposomal and extraliposomal space [37]. The transmission electron microscopy (TEM) image (Fig. 1b) showed uniform and spherical morphology of HAPO-1048 with an average diameter of 135.2 nm which was in accordance with the dynamic light scattering (DLS) measurement (Fig. 1c). Zeta potential of HAPO-1048 was –32.97 ± 2.36 mV, indicating the incorporation of HA (Fig. S1) and the encapsulation efficiency of IR-1048 in HAPO-1048 was 53.2% according to a previously reported method [32]. Moreover, the stability of HAPO-1048 in PBS and 10% fetal bovine serum (FBS) was evaluated by measuring the particle size changes. As shown in Fig. S2, the mean diameter of HAPO-1048 was kept in various aqueous media for 24 h and in PBS for 7 days without showing significant changes, suggesting a good stability for further long-term biomedical applications. The UV-vis spectrum of HAPO-1048 had two characteristic peaks around 930 nm and 1100 nm (Fig. 1d). These results were similar to those reported previously [32]. The temperature profiles of LIPO-1048 and HAPO-1048 solutions were recorded under the same condition (35 μg/mL, 1064 nm, 1 W/cm^2). Compared with PBS group, the temperatures of LIPO-1048 and HAPO-1048 were significantly raised (>25 °C) (Fig. 1e). However, there was no obvious difference in temperature between LIPO-1048 and HAPO-1048 and their photothermal conversion efficiencies were both around 41% (Fig. 1f, Fig. S3a and b), which confirmed that HA did not affect the photothermal properties of IR1048-loaded liposomes. The

temperature curve of HAPO-1048 under 1064 nm laser irradiation for five cycles showed obvious periodicity of change, demonstrating the excellent photothermal stability (Fig. S3c). Moreover, we could see that the temperature of HAPO-1048 increased with increasing concentration, which was conducive to subsequent PTT experiments (Fig. 1g).

2.2. *In vitro assessments for cellular uptake, cell viability and photothermal-induced cell killing effect of HAPO-1048/LIPO-1048 NPs*

CD44 is highly expressed in various kinds of tumor cells (such as UM-UC-3). CD44 functions as the major receptor molecule for HA and plays vital roles in promoting cancer cell growth, migration and metastasis [35,38,39]. Cellular uptake of liposomal complex (HAPO-1048 and LIPO-1048) is generally believed to be mediated by adsorption on the cell surface followed by endocytosis [40]. To assess the ability of cell uptake of HAPO-1048 NPs, UM-UC-3 cells were co-incubated with Cy5.5-HAPO-1048 or Cy5.5-LIPO-1048. The Cy5.5-HAPO-1048 group showed much stronger red fluorescence signals than those co-incubated with Cy5.5-LIPO-1048 (Fig. 2a), indicating that HA-based active targeting significantly increased the cellular uptake of Cy5.5-HAPO-1048. The obviously selective uptake of HAPO-1048 NPs was also verified by multicellular tumor spheroids (MCTs) (Fig. 2b). MCTs were used as a classical 3D model to mimic the transport of NPs in the microenvironment of tumors in vitro [41]. Compared to the weak fluorescence signals from 30 to 60 μm of MCTs in the Cy5.5-LIPO-1048 group, the Cy5.5-HAPO-1048 group exhibited stronger fluorescence intensity and deeper penetrating capability even at 60 μm, revealing the crucial role of HA in facilitating the selective uptake of Cy5.5-HAPO-1048 NPs. Subsequently, to evaluate the HAPO-1048/LIPO-1048 NPs-mediated photothermal killing of tumor cells in vitro, we used calcein-AM/PI co-staining assay to visualize the live (green) and dead (red) cells, and CCK-8 assay to quantify the cell viability after various treatments. Under the same condition (1064 nm, 1 W/cm^2, 6 min, $C_{IR\text{-}1048} = 2$ μg/mL), almost all cells were dead in the HAPO-1048 + Laser group, which exhibited a better cell killing effect than the LIPO-1048 + Laser group (Fig. 2c). It was also observed that non-laser groups (including PBS group, LIPO-1048 group and HAPO-1048 group) and PBS + Laser group had little effect on cell viability. In addition, the cell viability of UM-UC-3 decreased with increasing concentration as shown in Fig. 2d, also suggesting the excellent concentration-dependent photothermal effect. Besides, we evaluated the biocompatibility of HAPO-1048/LIPO-1048 NPs for normal human urothelial cells (SV-HUC-1). Negligible cell cytotoxicity was observed when the concentration was in the range of 0–200 μg/mL. Even at a high concentration up to 200 μg/mL for 24 h, the cell viabilities after HAPO-1048 and LIPO-1048 NPs treatments still more than 85% (88.77 ± 9.77% and 91.16 ± 1.09%, respectively) (Fig. 2e and f), demonstrating the low cytotoxicity of HAPO-1048 NPs and could be used for follow-up studies.

2.3. *Ultrasound-guided transurethral establishment of orthotopic BC model and monitoring of oxygenation dynamics with PA imaging*

From the schematic diagram and representative ultrasound images of scraping the bladder mucosa under ultrasound guidance, the main process of constructing a BC model can be vividly observed (Fig. 3a and 3b). Subsequently, we used functional PA imaging to monitor tissue oxygenation without labeling. At day 10 after model establishment, the average oxygen saturation of the arterial blood (SaO_2) was significantly increased and continuously increased until about day 18 (Fig. 3c and d), implying that there might be angiogenesis in the bladder tissue to supply oxygen. Previous research confirmed that the tumor growth beyond 1–2 mm in diameter requires the formation of new blood vessels to satisfy the high blood oxygen metabolic rates [42,43]. Bioluminescence imaging (BLI) confirmed the presence of a tumor in the bladder site (Fig. 3e). After euthanization, the whole bladder was excised to observe the bladder cavity. There was an abnormally proliferating tissue and H&E also confirmed the presence of BC. (Fig. 3f–h). These results indicated the successful establishment of orthotopic BC model under ultrasound guidance and the continuous, real-time monitoring of the dynamic change of SaO_2 during BC growth by functional PA imaging. Immunohistochemistry results showed the higher expression of CD44 in BC tissue than in normal bladder tissue (Fig. 3i) and this result was also confirmed at the cellular level [39].

2.4. *In vivo NIR-II OCTA imaging of orthotopic BC*

As mentioned above, tumor blood vessels play a vital role in supplying oxygenated blood and delivering materials to the tumor. OCTA is essentially the optical scattering of tissue that can observe changes in tumor blood vessels at the microscopic level and identify early-stage BC from within ultra-high-resolution structural imaging of tumors. We performed OCTA to image the surface blood vessels of normal and cancerous bladders on different days. As shown in Fig. 4a, the microvessels gradually decreased from the center to periphery in the area of tumor (the white dotted square) with a greater number and depth of blood vessels (the blue vessels on the images). In accordance with

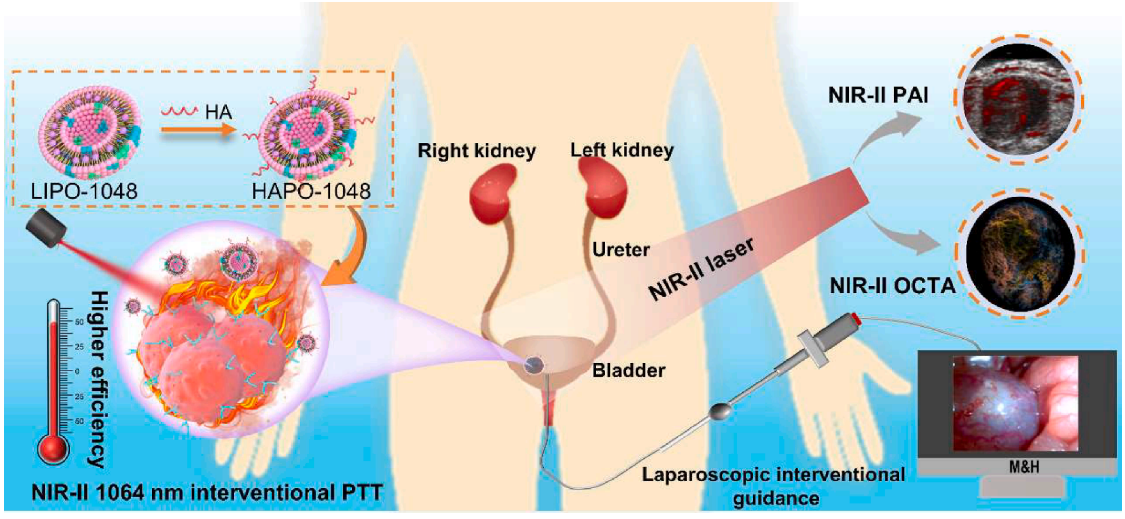

Scheme 1. Schematic representation of NIR-II optical imaging and non-invasive interventional photothermal therapy for BC. Dual modality NIR-II optical imaging allows the deeper guiding the NIR-II photothermal therapy for orthotopic BC *in vivo*.

previous studies [20], these results indicated that rapid tumor growth leads to microvascular morphometric changes and tumor angiogenesis. Subsequently, we analyzed structural image (Fig. 4a) obtained from the tissue cross-section. The bladder is mainly divided into the mucosa, lamina propria and muscularis. As shown in Fig. 4b, we can clearly distinguish different layers of structures in OCTA. In a normal bladder, each layer maintains its structural integrity (Fig. 4b i). However, in case of BC, the tumor in the bladder wall gradually invades all the layers of bladder tissue, leading to structural disorder, while structures far from the tumor area remain relatively intact. (Fig. 4b ii–iiic). Unlike PA, OCTA provides microvascular changes and ultra-high-resolution structural imaging of tumors during early tumor growth, which can serve as a powerful tool to collaborate with PA at the microscopic level in order to provide valuable information on early micro-BC diagnoses in the clinic.

2.5. NIR-II PAI of orthotopic BC

NIR-II optical bioimaging is of growing interest in orthotopic tumor diagnosis owing to its advantages of deep tissue penetration, low light scattering, and an enhanced signal-to-background ratio (SBR) when compared to the traditional NIR-I region [14,44,45]. To evaluate the PAI capability of HAPO-1048 in the NIR-II region, overlaid PA/US images with HAPO-1048 were acquired at different wavelengths (including 750, 808, and 970 nm) in chicken breast tissues (Fig. 5a, b and Fig. S4a). It could be seen that choosing 970 nm wavelength had a more obvious photoacoustic signal when the thickness of the chicken breast tissue was about 4.92 mm (Fig. 5a). By quantifying the SBR of Fig. 5a, the SBR value at 970 nm (NIR-II region) was found to be 5.66 ± 0.097, which was nearly two times more than those at 750 and 808 nm (NIR-I region) (Fig. 5b). These results indicate that using HAPO-1048 as the PAI contrast agent at 970 nm could offer superior PA imaging contrast, imaging depth, and SBR. Thus, we chose the 970 nm wavelength for the next PAI experiment for orthotopic BC imaging. As shown in Fig. 4C, the PA signals of HAPO-1048 increased linearly with an increase in concentration within the range of 10–200 μg/mL ($R^2 = 0.9951$). To assess the NIR-II PAI *in vivo*, we selected mice whose tumors were growing from the upper mucosa of the bladder and enlarged up to the lower mucosa of the bladder. As shown in Fig. 5d, the tumor was roughly 4.38 mm in depth, which was sufficient to be evaluated by the NIR-II PAI without causing severe dysuria and pain to the mice. *In vivo* PAI images were acquired before and 3, 6, 12, 24, 48, and 72 h after the i.v. injection of HAPO-1048 (200 μg/mL). The PA signal in the tumor region gradually increased with time and reached its peak at 24 h post injection (Fig. S4b). Using the laser excitation of 970 nm, NIR-II PAI showed a 4.38 mm-deep signal, which was not possible to achieve effectively with the NIR-I laser excitation. This also underlined the advantage of using an NIR-II PAI to visualize an orthotopic tumor. From the result, we also noticed that HAPO-1048 was more enriched in the periphery of the

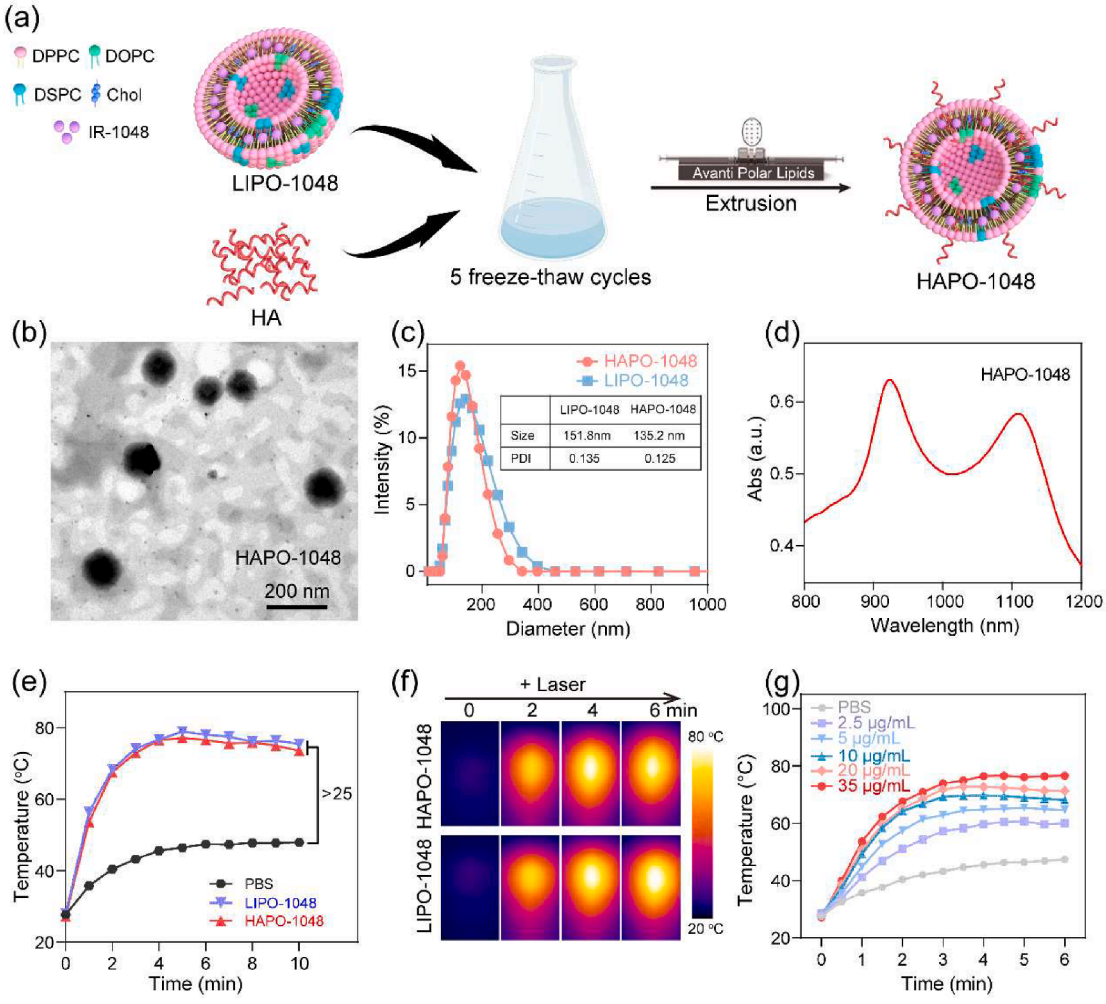

Fig. 1. Characterization and temperature measurements of HAPO-1048. (a) Illustration of the preparation procedures of HAPO-1048. (b) TEM images of the HAPO-1048 NPs. (c) Hydrodynamic diameters of LIPO-1048 and HAPO-1048 measured by DLS. (d) Typical UV-vis spectrum of HAPO-1048. (e) Heating curves of PBS (black), LIPO-1048 (blue) and HAPO-1048 (red) (35 μg/mL, 1064 nm, 1 W/cm^2). (f) Corresponding photographs of LIPO-1048 and HAPO-1048 in Fig. 1e. (g) Heating curves of HAPO-1048 under different concentrations.

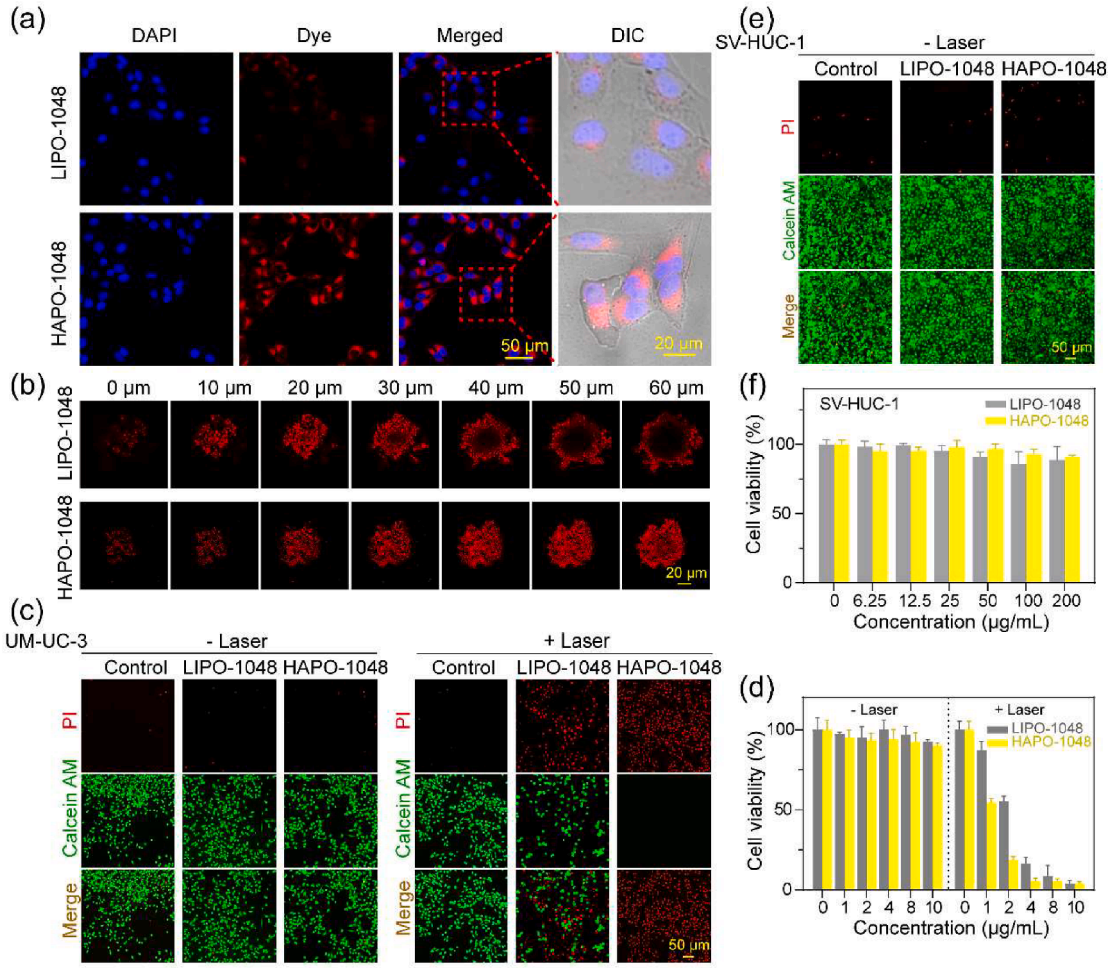

Fig. 2. In vitro cell evaluation. (a) CLSM images of UM-UC-3 cells after incubation with NPs for 6 h (blue, nuclei stained with DAPI; red, HAPO-1048/LIPO-1048 labeled with Cy5.5). Scale bar, 50 μm (20 μm for inset). (b) Penetration ability of HAPO-1048 and LIPO-1048 into MCTs for 24 h. Scale bar, 100 μm. (C) Live/dead cell imaging of UM-UC-3 cells costained with calcein-AM (live cells, green) and PI (dead cells, red). (d) UM-UC-3 cell viability after being treated with different concentrations of HAPO-1048/LIPO-1048 (1064 nm, 1 W/cm^2, 6 min). (e) Live/dead cell imaging of SV-HUC-1 cells costained with calcein-AM (live cells, green) and PI (dead cells, red). (f) SV-HUC-1 cell viability after being treated with different concentrations of HAPO-1048/LIPO-1048 (1064 nm, 1 W/cm^2, 6 min). *$p < 0.05$, **$p < 0.01$ versus control. All bars represent the mean ± s.d. ($n = 5$/group).

tumor, which could be due to the dense tumor stroma and differential distribution of vessels between the tumor center and tumor periphery. The high density of tumor stroma around the tumor that limits the drug delivery to tumor tissues, blood vessels and the center of tumor [46,47]. The varying distribution of blood vessels affects drug delivery. In other words, the targeting effect relies on the blood supply of the tissue [48].

By exploiting the high contrast between endogenous or exogenous agents, PA can sensitively detect early tiny tumors. As demonstrated in our previous study, PAI can detect hepatic melanoma using the same PA system [43]. Wang *et al.* reported that their three-dimensional (3D)-PACT system can detect a tumor of 1 mm-diameter, but it's only embedded in the breast-mimicking phantom [49], As shown in Fig. 5e, PAI detected orthotopic BC as small as approximately 2 mm in diameter orthotopic BC *in vivo*, which was smaller than the result of previous research [50]. We used software to reconstruct 3D US/PA images in order to better display the 3D morphology of the bladder tumor and the enrichment of PA signals of HAPO-1048 in the entire tumor region (Fig. 5f and Fig. S5). The 3D-rendered PA images showed that the PA signals of HAPO-1048 peaked at 24 h, which corresponded to 2D PAI. Additionally, since the bladder is an organ that stores urine, the dynamic changes of the entire bladder and tumor were vividly displayed from the 3D views. In general, PAI is an effective, non-invasive, real-time, and highly-sensitive method for imaging early-stage tiny tumors and to achieve long-term surveillance, especially in NIR-II region, which has the advantages of greater depth and higher SBR.

2.6. *Minimally invasive interventional PTT for orthotopic BC*

The white light (WL) image-guided TURBT is the standard intervention following an initial diagnosis of NMIBC [51]. Based on the existing clinical imaging technologies, we aimed to design the minimally invasive interventional PTT system containing a laparoscope in order to intuitively provide the general condition outside the bladder and an ultrasound to guide the intravesical treatment. Fig. 6a illustrates the minimally invasive interventional PTT system.

As shown in Fig. 6b and 6c, at 24 h after the tail-vein injection of HAPO-1048 NPs (200 μg/mL, 200 μL), interventional PTT for BC was executed. Laparoscopically, the general condition of tumor (yellow arrow) could be observed prominently and an ultrasound was utilized to assist the intravesical PTT. Noticeably, after 6 min of PTT, the tumor in the bladder cavity was ablated. Subsequently, as observed through laparoscopy, a distinct burn could be observed on the tumor tissues of bladder (Fig. S6a). Furthermore, H&E staining of tumor sections showed that the nuclei were shrunk and the tumor cells were destroyed (Fig. S6b). The temperature changes of different groups (including 200 μg/mL, 200 μL of HAPO-1048 and LIPO-1048, and 200 μL of PBS) *in vivo*

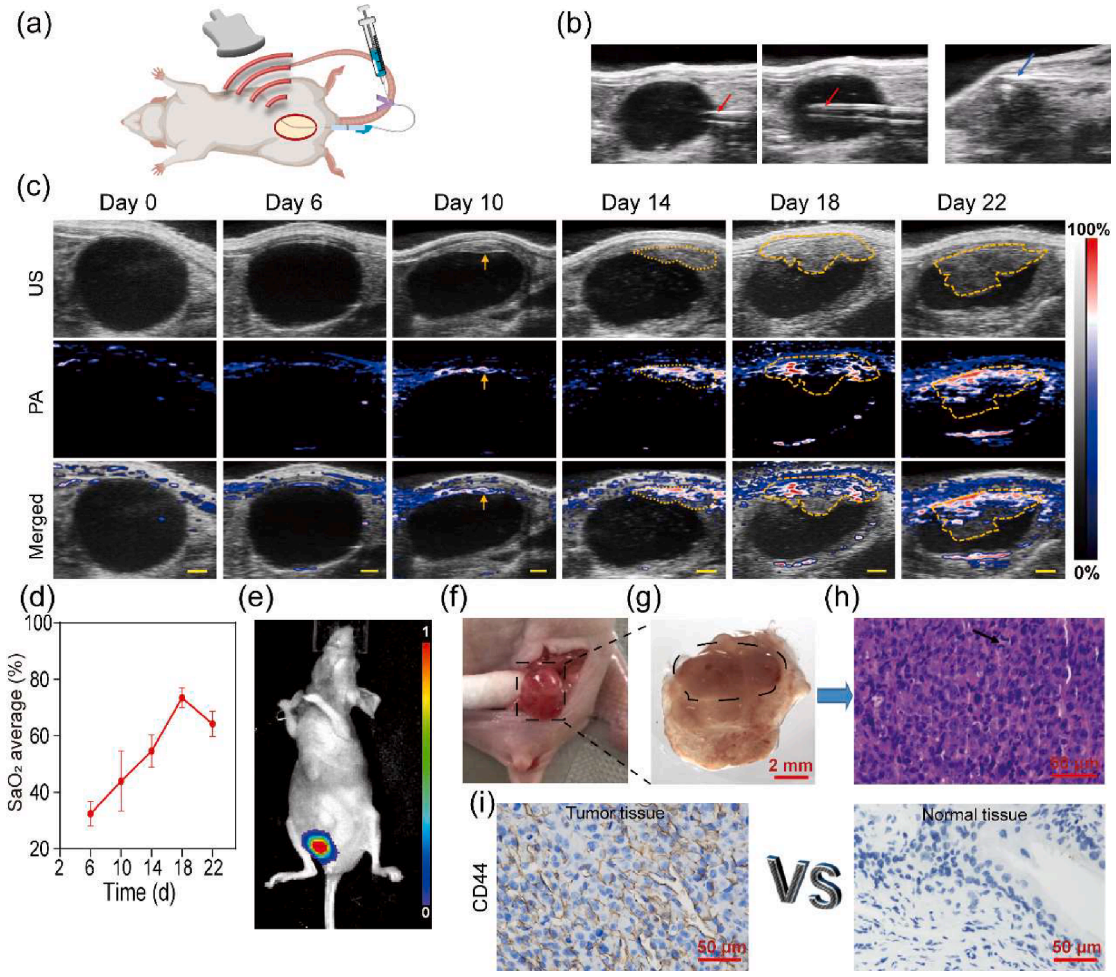

Fig. 3. The Construction of orthotopic BC model (a) Illustration of Ultrasound-guided transurethral establishment of orthotopic BC model. (b) US images of scraping the upper bladder mucosa upon ultrasound guidance. The arrows represent 24-gauge plastic catheter (red) and needle (blue). (c) Monitoring of tissue blood oxygenation from day 0 to 22 after constructing models by PAI. The yellow arrows and circles represent the region of interest. Scale bars, 1 mm. (d) Quantification of average SaO_2 over time (n = 3). (e) Tumor establishment was confirmed by bioluminescence image. (f) Representative anatomic observation of bladder before excision from the mouse abdominopelvic cavity. (g) The excised bladder was cut open to capture the gross anatomopathological changes. Scale bar, 2 mm. (h) Representative pathological examination by H&E. Scale bar, 50 μm. (i) Representative CD44 immunohistochemistry for comparing the expression of CD44 in normal tissues and tumor tissues. Scale bar, 50 μm.

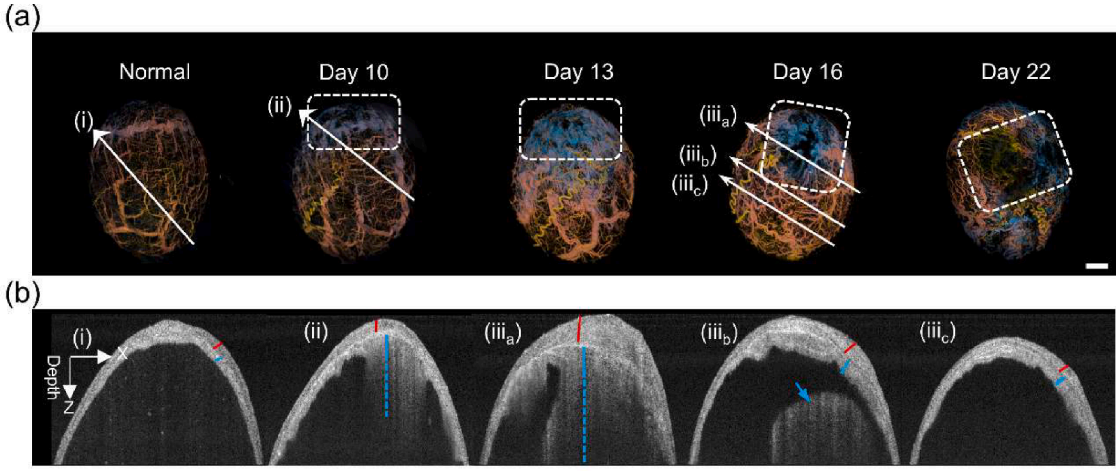

Fig. 4. *In vivo* OCTA imaging. (a) Representative OCTA images of normal and tumorous bladders at different time points. The white dotted square represents the tumor area. Scale bar, 1 mm. (b) Representative tissue cross section structural image from Fig. 4a. The red lines represent muscularis tissues; the blue lines represent urothelium and lamina propria tissues. The depth of images is 2 mm.

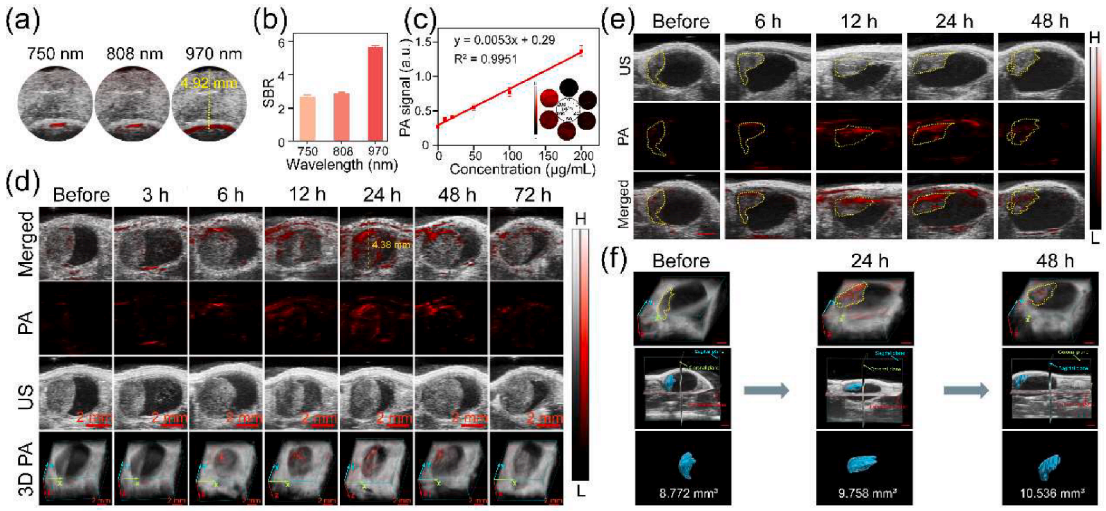

Fig. 5. NIR-II photoacoustic imaging. (a) PA images of HAPO-1048 NPs embedded in chicken breast with different wavelengths (750, 808, and 970 nm). The yellow dashed line represented the depth of the detected signal (depth ≈ 4.92 mm). (b) Corresponding signal-to-background ratio of (a). (c) Linear plot of PA signal versus concentration of HAPO-1048 NPs (0, 10, 20, 50, 100, and 200 μg/mL, respectively). The inset was PA images of HAPO-1048 at various concentrations. (d) *In vivo* PA/US and 3D-rendered PA images of deep bladder cancer with intravenous injection of HAPO-1048 at different time points. (e) Bladder microtumor (diameter ≈ 2 mm) was sensitively detected by PAI. Scale bar, 1 mm. (f) Corresponding *in vivo* 3D-rendered PA images and 3D reconstruction of tumor of (e). Scale bar, 1 mm. All error bars represent the mean ± s.d. (n = 3).

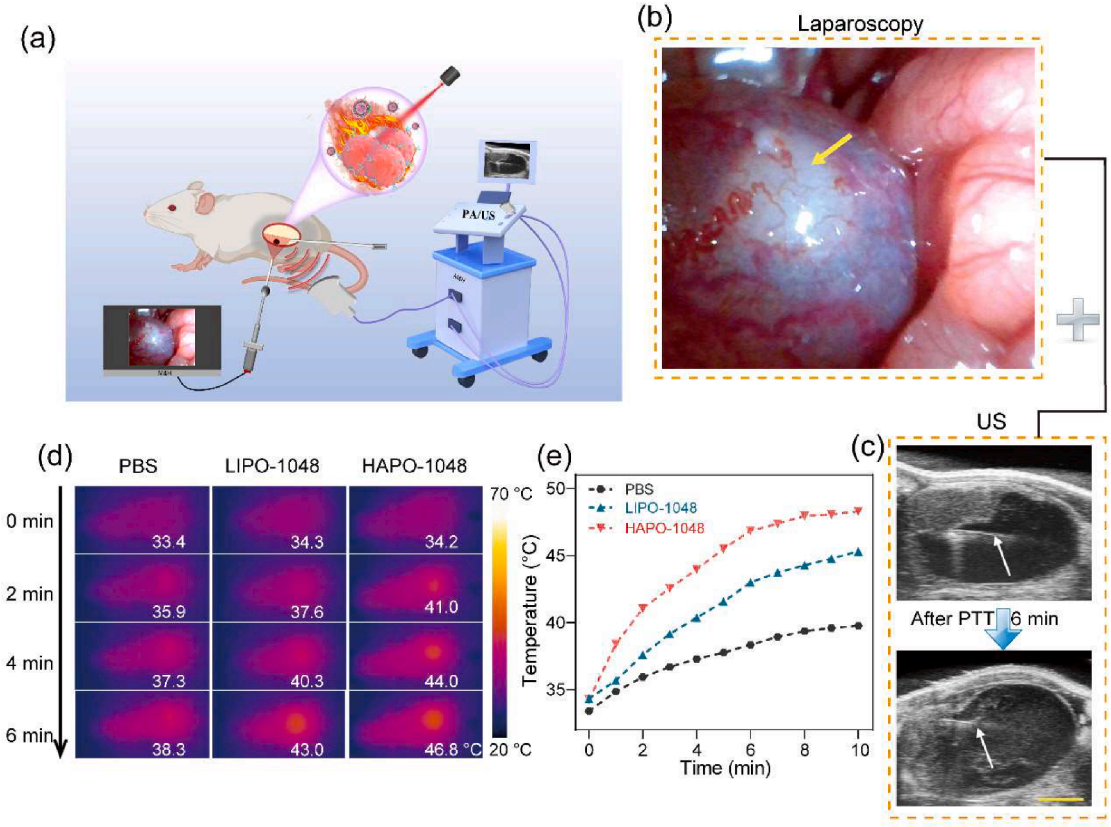

Fig. 6. Process of minimally invasive interventional PTT. (a) Illustration of minimally invasive interventional PTT. (b) Laparoscopic exploration of bladder tumor. The yellow arrow pointed to the location of the tumor. (c) Ultrasound-guided optical fiber for the intravesical PTT. The white arrows represented the optical fiber. Scale bar, 1 mm. (d) Infrared thermal images of tumor-bearing mice before and after PTT (1064 nm, 1 W/cm^2). (e) Corresponding temperature change curves of (d).

were also recorded (Fig. 6d). Due to heterogeneity of tumors and laser attenuation in tissue, the photothermal temperature would be affected *in vivo* [52,53]. Compared with PBS group (≈ 38.3 °C) and LIPO-1048 group (≈ 43.0 °C), the tumor temperature in the HAPO-1048 group showed higher elevation and reached up to ≈ 46.8 °C within 6 min, leading to more effective tumor ablation. The corresponding temperature change curves of Fig. 6d was recorded (Fig. 6e). These results suggest that minimally invasive interventional PTT can be a promising technology to visualize PTT of BC.

BLI was applied to monitor the therapeutic effect after NIR-II PTT

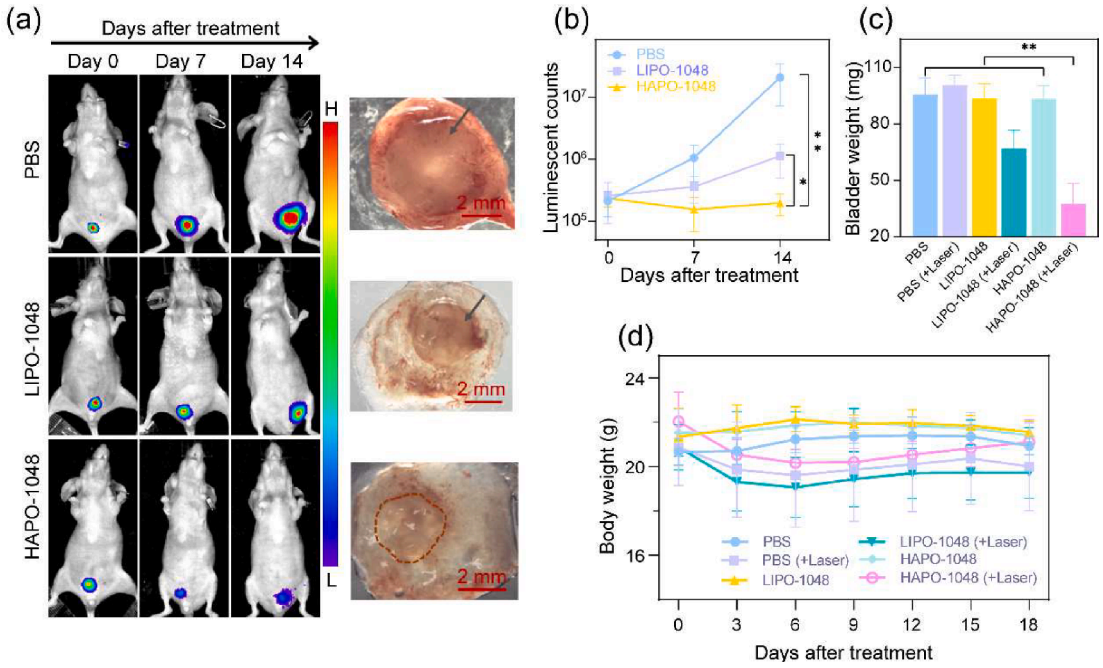

Fig. 7. Evaluation of therapeutic efficacy. (a) Representative bioluminescence images and photographs of mouse bladder in different groups (n = 5 to 7 per group) (scale bar = 2 mm, the gray arrows and circle represent the region of tumor). (b) Quantitative analysis of bioluminescence signals in a. The data represent the mean ± s.d. (*P < 0.05, **P < 0.01). (c) Excised bladder weight of different groups at end point (n = 3 to 5 per group). (d) Body weight of tumor-bearing mice after different treatments (n = 3 to 5 per group).

(Fig. 7a). Compared to the PBS + Laser group, the BLI signals of the LIPO-1048 + Laser group on the 14th day after therapy was reduced, which could be primarily attributed to the therapeutic effect caused by passive targeting. Notably, the HAPO-1048 + Laser group showed a better efficacy in tumor suppression. The corresponding photographs of the mouse bladder in Fig. 7a also demonstrated these results. As shown

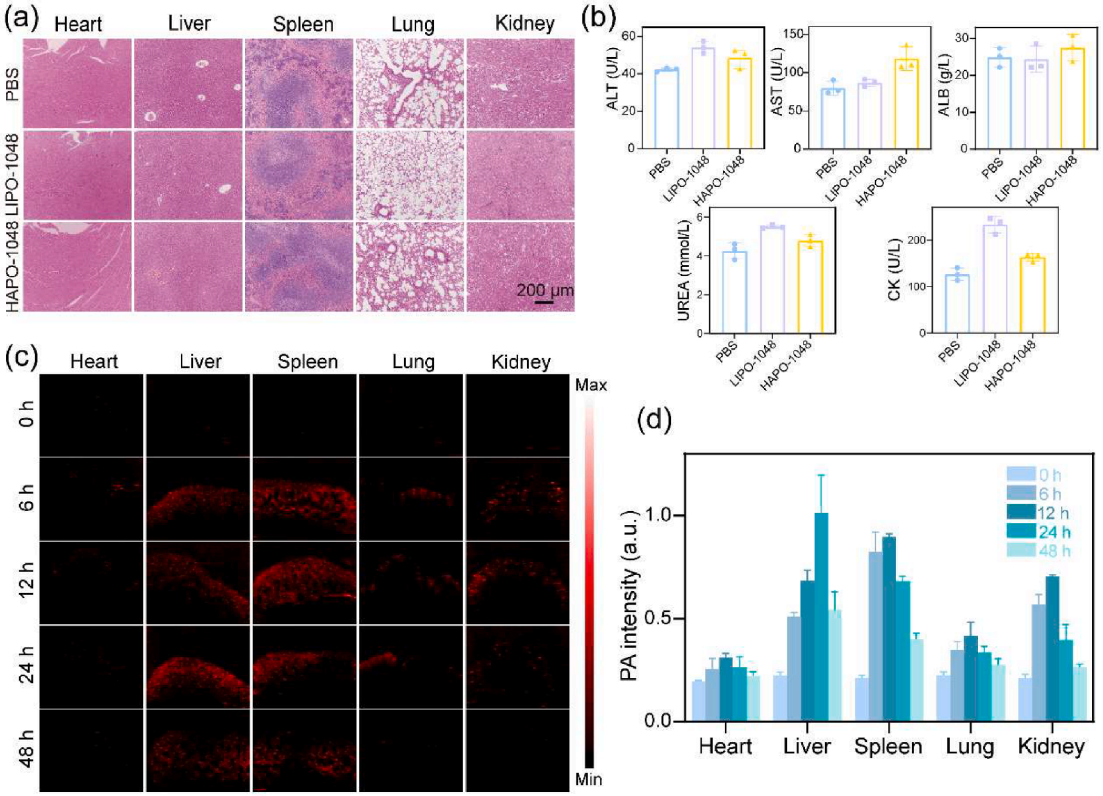

Fig. 8. *In vivo* biosafety of HAPO-1048. (a) Representative H&E-stained images of the major organs and (b) hematological analysis on day 14 after injection of HAPO-1048, LIPO-1048 (200 μg/mL, 200 μL) and PBS respectively. (c) PA images of major organs of healthy mice at different time points after injection of HAPO-1048 (200 μg/mL, 200 μL) and (d) the corresponding PA intensity. All bars represent the mean ± s.d. (n = 6).

in Fig. 7a, after 14 days of PTT treatment, the stripped tumors were collected for magnification observation under stereoscopic microscope (Leica M165 FC, Germany). The clear representative images of the orthotopic bladder cancer shown a significant tumor suppression in HAPO-1048 plus laser-treated group, confirming a more effective treatment effect than the other groups. The results of quantitative BLI analysis revealed that HAPO-1048 + Laser inhibited the tumor growth more effectively than the other groups (Fig. 7b). Similarly, the tumor burden by bladder weights and tumor growth inhibition were also measured (Fig. 7c and Fig. S7). All of these results indicate that the overall therapeutic effect due to the active targeting of HAPO-1048-mediated PTT was effective. The surgical trauma and tumor progression are the main factors for loss of body weight, which needs to be monitored [29]. As shown in Fig. 7d, all of the Laser groups showed a slight decrease in weight within 3–6 days, which may be a consequence of the discomfort of mice caused by insertion of the laparoscope into the abdomen and the fiber inserted though the urethra. During the subsequent 9–18 days of monitoring, the mice gradually recovered their weights. In the other non-laser groups, there was no significant difference in the weight. We speculated that it might be caused by the tumor, which was mainly confined and grown in the bladder cavity, affecting the excretion of urine.

2.7. *In vivo safety evaluation of NIR-II HAPO-1048 PTT agents*

At 14 days after systemic administration of HAPO-1048, LIPO-1048 (200 μg/mL, 200 μL) and PBS (200 μL), there was no obvious apoptosis/necrosis in the major organs (Fig. 8a), and the hematological analysis showed that they were within the normal range (Fig. 8b). Additionally, the major organs of healthy mice were collected to evaluate the biodistribution by PAI at 0, 6, 12, 24, and 48 h after intravenous injection of HAPO-1048 NPs (Fig. 8c). PA intensities of major organs were quantified in Fig. 8d: It showed that the liver and spleen significantly increased at 24 h and decreased at 48 h post-injection, revealing that the NPs were primarily accumulated in the liver and spleen after being injected intravenously and cleared *via* hepatobiliary elimination. Moreover, the rate of hemolysis after incubation with HAPO-1048, even at a concentration of 300 μg/mL, was less than the prescribed upper value of the hemolysis index (5%) (Fig. S8). All these results demonstrated the excellent biocompatibility of HAPO-1048 for fundamental and preclinical studies.

3. Conclusion

In summary, we synthesized a versatile liposomal complex functionalized with IR-1048 and HA (HAPO-1048 NPs) to enable BC-targeting and NIR-II phototheranostics. This study demonstrated that HAPO-1048: (i) has an exceptional NIR-II PAI ability to image deeper orthotopic BC *in vivo* and (ii) is able to detect early micro-bladder tumors with high sensitivity and specificity. Moreover, we also introduced the NIR-II OCTA to observe the changes of tumor blood vessels at the microscopic level and combined with PA to identify early-stage BC using ultra-high-resolution microvessel structural imaging of tumors. The multimodal NIR-II PA and OCTA provided high-contrast, high-sensitivity BC anatomy and function with in-depth information and sub-micrometer resolution, which would be a promising avenue for early micro-BC detection. It is worth mentioning that prior to the start of *in vivo* experiments, ultrasound-guided transurethral establishment of orthotopic BC model was constructed, which could provide an experimental reference for accurate model-construction in the future. Interestingly, the same idea of accuracy was also applied to the treatment. We developed an intervention-guided PTT system based on laparoscopy and ultrasound to visualize NIR-II PTT, which was also minimally invasive for orthotopic BC theranostics. However, due to the limited urethral diameter of experimental animals, the laparoscope can only be accessed through the abdomen. In the future, it will be possible to achieve guidance and therapy through the urethra into the bladder at the same time on the larger animal model. Overall, our study offers a strategy for studying early-stage micro-sized tumors using the NIR-II optical imaging and minimally-invasive intervention of NIR-II PTT in orthotopic BC, which we believe holds significant potential for other urinary system diseases as well.

Declaration of Competing Interest

The authors declare that they have no known competing financial interests or personal relationships that could have appeared to influence the work reported in this paper.

Data availability

Data will be made available on request.

Acknowledgments

This work was supported by the Natural science Foundation of Guangdong Province (2021A1515011654), Fundamental Research Funds for the Central Universities of China (20720210117), Joint Funds for the Innovation of Science and Technology of Fujian province (2019Y9128), National Natural Science Foundation of China (81971665), Natural Science Foundation of Fujian Province (2021J05006, 2021J011366), Medical and Health Guidance Project of Xiamen (3502Z20214ZD1016), and Xiamen Health High-Level Talent Training Program. Xiamen Key Laboratory of Endocrine-Related Cancer Precision Medicine (XKLEC2021KF03, XKLEC2020KF04). Key Laboratory of OptoElectronic Science and Technology for Medicine of Ministry of Education, Fujian Provincial Key Laboratory of Photonics Technology (JYG2105). XMU Undergraduate Innovation and Entrepreneurship Training Programs ((202210384051 , S202210384404 , 2021X1119, 2021Y1119, S202110384391), and Shenzhen Bay Laboratory (SZBL2019062801005).

Appendix A. Supplementary data

Supplementary data to this article can be found online at https://doi.org/10.1016/j.cej.2022.137846.

References:

[1] J. Ferlay, M. Colombet, I. Soerjomataram, D.M. Parkin, M. Piñeros, A. Znaor, F. Bray. Cancer statistics for the year 2020: An overview. Int. J. Cancer. 149 (2021) 778-789.

[2] E. Compérat, S. Larré, M. Roupret, Y. Neuzillet, G. Pignot, H. Quintens, N. Houéde, C. Roy, X. Durand, J. Varinot, D. Vordos, M. Rouanne, M.A. Bakhri, P. Bertrand, S. C. Jeglinschi, O. Cussenot, M. Soulié, C. Pfister, Clinicopathological characteristics of urothelial bladder cancer in patients less than 40 years old, Virchows Arch. 466 (2015) 589–594.

[3] M. Babjuk, M. Burger, O. Capoun, D. Cohen, E.M. Compérat, J.L. Dominguez Escrig, P. Gontero, F. Liedberg, A. Masson-Lecomte, A.H. Mostafid, J. Palou, B.W. G. van Rhijn, M. Rouprêt, S.F. Shariat, T. Seisen, V. Soukup, R.J. Sylvester, European association of urology guidelines on non–muscle-invasive bladder cancer (Ta, T1, and carcinoma in situ), European Urology. 81 (1) (2022) 75–94.

[4] R.T. Bryan, W. Liu, S.J. Pirrie, R. Amir, J. Gallagher, A.I. Hughes, K.P. Jefferson, A. Knight, V. Nanton, H.P. Mintz, A.M. Pope, J.W.F. Catto, P. Patel, N.D. James, Comparing an imaging-guided pathway with the standard pathway for staging muscle-invasive bladder cancer: preliminary data from the bladder path study, European Urology. 80 (2021) 12–15.

[5] M.C. Kriegmair, J. Rother, B. Grychtol, M. Theuring, M. Ritter, C. Günes, M. S. Michel, N.C. Deliolanis, C. Bolenz, Multiparametric cystoscopy for detection of bladder cancer using real-time multispectral imaging, European Urology. 77 (2) (2020) 251–259.

[6] V. Soukup, O. Čapoun, D. Cohen, V. Hernández, M. Burger, E. Compérat, P. Gontero, T. Lam, A.H. Mostafid, J. Palou, B.W.G. van Rhijn, M. Rouprêt, S. F. Shariat, R. Sylvester, Y. Yuan, R. Zigeuner, M. Babjuk, Risk stratification tools and prognostic models in non–muscle-invasive bladder cancer: A critical assessment from the european association of urology non-muscle-invasive bladder cancer guidelines panel, European Urology, Focus. 6 (2020) 479–489.

[7] N. Yoshida, H. Doyama, T. Yano, T. Horimatsu, N. Uedo, Y. Yamamoto, N. Kakushima, H. Kanzaki, S. Hori, K. Yao, I. Oda, C. Katada, C. Yokoi, K. Ohata,

K. Yoshimura, H. Ishikawa, M. Muto, Early gastric cancer detection in high-risk patients: a multicentre randomised controlled trial on the effect of second-generation narrow band imaging, Gut. 70 (2021) 67–75.
[8] C. Zheng, Y. Lv, Q. Zhong, R. Wang, Q. Jiang, Narrow band imaging diagnosis of bladder cancer: systematic review and meta-analysis: systematic review and meta-analysis, BJU International. 110 (2012) E680-E687.
[9] B. Kiss, N.S. van den Berg, R. Ertsey, K. McKenna, K.E. Mach, C.A. Zhang, J.-P. Volkmer, I.L. Weissman, E.L. Rosenthal, J.C. Liao, CD47-targeted near-infrared photoimmunotherapy for human bladder cancer, Clin Cancer Res. 25 (2019) 3561-3571.
[10] L.V. Wang, S. Hu, Photoacoustic tomography: in vivo imaging from organelles to organs, Science. 335 (2012) 1458–1462.
[11] L.V. Wang, J. Yao, A practical guide to photoacoustic tomography in the life sciences, Nat Methods. 13 (8) (2016) 627–638.
[12] K.S. Valluru, K.E. Wilson, J.K. Willmann, Photoacoustic imaging in oncology: translational preclinical and early clinical experience, Radiology. 280 (2016) 332–349.
[13] S. Zhang, H. Chen, L. Wang, X. Qin, B.-P. Jiang, S.-C. Ji, X.-C. Shen, H. Liang, A general approach to design dual ratiometric fluorescent and photoacoustic probes for quantitatively visualizing tumor hypoxia levels in vivo, Angewandte Chemie. 134 (2022) e202107076.
[14] G. Song, M. Kenney, Y.-S. Chen, X. Zheng, Y. Deng, Z. Chen, S.X. Wang, S. S. Gambhir, H. Dai, J. Rao, Carbon-coated FeCo nanoparticles as sensitive magnetic-particle-imaging tracers with photothermal and magnetothermal properties, Nat Biomed Eng. 4 (3) (2020) 325–334.
[15] Z. Lei, F. Zhang, Molecular engineering of NIR-II fluorophores for improved biomedical detection, Angew. Chem. Int. Ed. 60 (30) (2021) 16294–16308.
[16] Y. Li, X. Fan, Y. Li, L. Zhu, R. Chen, Y. Zhang, H. Ni, Q. Xia, Z. Feng, B.Z. Tang, J. Qian, H. Lin, Biologically excretable AIE nanoparticles wear tumor cell-derived "exosome caps" for efficient NIR-II fluorescence imaging-guided photothermal therapy, Nano Today. 41 (2021), 101333.
[17] C. Zhu, Z. Ding, Z. Guo, X. Guo, A. Yang, Z. Li, B.-P. Jiang, X.-C. Shen, Full-spectrum responsive ZrO2-based phototheranostic agent for NIR-II photoacoustic imaging-guided cancer phototherapy, Biomater. Sci. 8 (23) (2020) 6515–6525.
[18] C. Scheepbouwer, S. Meyer, M.J. Burggraaf, J. Jose, C.F.M. Molthoff, R. M. Hoffman, A multimodal imaging approach for longitudinal evaluation of bladder tumor development in an orthotopic murine model, PLoS ONE. 11 (8) (2016) e0161284.
[19] B. Park, K.M. Lee, S. Park, M. Yun, H.-J. Choi, J. Kim, C. Lee, H. Kim, C. Kim, Deep tissue photoacoustic imaging of nickel(II) dithiolene-containing polymeric nanoparticles in the second near-infrared window, Theranostics. 10 (6) (2020) 2509–2521.
[20] D. Huang, G. Wang, J. Mao, C. Liu, Z. Fan, Y. Zhang, B. Zhang, Y. Zhao, C. Dai, Y. He, H. Ma, G. Liu, X. Chen, Q. Zhao, Intravital whole-process monitoring thermo-chemotherapy via 2D silicon nanoplatform: A macro guidance and long-term microscopic precise imaging strategy, Adv. Sci. 8 (2021) 2101242.
[21] E.C.C. Cauberg, D.M. de Bruin, D.J. Faber, T.G. van Leeuwen, J.J.M.C.H. de la Rosette, T.M. de Reijke, A new generation of optical diagnostics for bladder cancer: technology, diagnostic accuracy, and future applications, European Urology. 56 (2009) 287–297.
[22] E. Zagaynova, M.J. Manyak, O. Streltsova, N. Gladkova, F. Feldchtein, V. Kamensky, A multicenter study of optical coherence tomography for diagnosis and guided surgery of bladder cancer, JCO. 22 (14_suppl) (2004) 4538.
[23] V.P. Nguyen, W. Qian, Y. Li, B. Liu, M. Aaberg, J. Henry, W. Zhang, X. Wang, Y. M. Paulus, Chain-like gold nanoparticle clusters for multimodal photoacoustic microscopy and optical coherence tomography enhanced molecular imaging, Nat Commun. 12 (2021) 34.
[24] X. Zhao, C.-X. Yang, L.-G. Chen, X.-P. Yan, Dual-stimuli responsive and reversibly activatable theranostic nanoprobe for precision tumor-targeting and fluorescence-guided photothermal therapy, Nat Commun. 8 (2017) 14998.
[25] M. Burger, H.B. Grossman, M. Droller, J. Schmidbauer, G. Hermann, O. Drăgoescu, E. Ray, Y. Fradet, A. Karl, J.P. Burgués, J.A. Witjes, A. Stenzl, P. Jichlinski, D. Jocham, Photodynamic diagnosis of non–muscle-invasive bladder cancer with hexaminolevulinate cystoscopy: A meta-analysis of detection and recurrence based on raw data, European Urology. 64 (2013) 846–854.
[26] F. Zhang, X. Han, Y. Hu, S. Wang, S. Liu, X. Pan, H. Wang, J. Ma, W. Wang, S. Li, Q. Wu, H. Shen, X. Yu, Q. Yuan, H. Liu, Interventional photothermal therapy enhanced brachytherapy: A new strategy to fight deep pancreatic cancer, Adv. Sci. 6 (2019) 1801507.
[27] S. Hong, D.-W. Zheng, C. Zhang, Q.-X. Huang, S.-X. Cheng, X.-Z. Zhang, Vascular disrupting agent induced aggregation of gold nanoparticles for photothermally enhanced tumor vascular disruption, Sci Adv. 6 (2020) eabb0020.
[28] D. Liu, L. Ma, Y. An, Y.u. Li, Y. Liu, L.u. Wang, J. Guo, J. Wang, J. Zhou, Thermoresponsive nanogel-encapsulated PEDOT and HSP70 inhibitor for improving the depth of the photothermal therapeutic effect, Advanced Functional Materials. 26 (26) (2016) 4749.
[29] Q. Li, K. Chen, W. Huang, H. Ma, X. Zhao, J. Zhang, Y. Zhang, C. Fang, L. Nie, Minimally invasive photothermal ablation assisted by laparoscopy as an effective preoperative neoadjuvant treatment for orthotopic hepatocellular carcinoma, Cancer Letters. 496 (2021) 169–178.
[30] X.Y. Wong, A. Sena-Torralba, R. Álvarez-Diduk, K. Muthoosamy, A. Merkoçi, Nanomaterials for nanotheranostics: tuning their properties according to disease needs, ACS Nano. 14 (2020) 2585–2627.
[31] L.C. Noukeu, J. Wolf, B. Yuan, S. Banerjee, K.T. Nguyen, Nanoparticles for detection and treatment of peripheral arterial disease, Small. 14 (2018) 1800644.
[32] X. Geng, D. Gao, D. Hu, Q. Liu, C. Liu, Z. Yuan, X. Zhang, X. Liu, Z. Sheng, X. Wang, H. Zheng, Active-targeting NIR-II phototheranostics in multiple tumor models using platelet-camouflaged nanoprobes, ACS Appl. Mater. Interfaces. 12 (50) (2020) 55624–55637.
[33] H. Lee, C. Song, Y.S. Hong, M.S. Kim, H.R. Cho, T. Kang, K. Shin, S.H. Choi, T. Hyeon, D.-H. Kim, Wearable/disposable sweat-based glucose monitoring device with multistage transdermal drug delivery module, Sci Adv. 3 (2017) e1601314.
[34] Z. Luo, Y. Dai, H. Gao, Development and application of hyaluronic acid in tumor targeting drug delivery, Acta Pharmaceutica Sinica B. 9 (6) (2019) 1099–1112.
[35] C. Zhu, Z. Guo, A. Yang, B.-P. Jiang, H. Liang, X.-C. Shen, The precise anti-tumor effect of a metallopolysaccharide-based nanotheranostic: turning phototherapy into programmed chemotherapy, Inorganic Chemistry, Frontiers. 9 (2022) 1869–1878.
[36] B.o. Zhou, B.-P. Jiang, W. Sun, F.-M. Wei, Y. He, H. Liang, X.-C. Shen, Water-dispersible prussian blue hyaluronic acid nanocubes with near-infrared photoinduced singlet oxygen production and photothermal activities for cancer theranostics, ACS Appl. Mater. Interfaces. 10 (21) (2018) 18036–18049.
[37] A.P. Costa, X. Xu, D.J. Burgess, Freeze-anneal-thaw cycling of unilamellar liposomes: effect on encapsulation efficiency, Pharm Res. 31 (2014) 97–103.
[38] W.-L. Wang, Z. Guo, Y.u. Lu, X.-C. Shen, T. Chen, R.-T. Huang, B.o. Zhou, C. Wen, H. Liang, B.-P. Jiang, Receptor-mediated and tumor-microenvironment combination-responsive Ru nanoaggregates for enhanced cancer phototheranostics, ACS Appl. Mater. Interfaces. 11 (19) (2019) 17294–17305.
[39] M. Ahmed, J. Sottnik, G. Dancik, D. Sahu, D. Hansel, D. Theodorescu, M. Schwartz, An osteopontin/CD44 axis in RhoGDI2-mediated metastasis suppression, Cancer Cell. 30 (3) (2016) 432–443.
[40] Y. Chi, X. Yin, K. Sun, S. Feng, J. Liu, D. Chen, C. Guo, Z. Wu, Redox-sensitive and hyaluronic acid functionalized liposomes for cytoplasmic drug delivery to osteosarcoma in animal models, Journal of Controlled Release. 261 (2017) 113–125.
[41] W. Lin, H. Liu, L. Chen, J. Chen, D. Zhang, Q. Cheng, F. Yang, Q. Zeng, T. Chen, Pre-clinical MRI-guided intravesical instillation theranosis of bladder cancer by tumor-selective oxygen nanogenerator, Nano Today. 38 (2021), 101124.
[42] S. Bellou, E. Karali, E. Bagli, N. Al-Maharik, L. Morbidelli, M. Ziche, H. Adlercreutz, C. Murphy, T. Fotsis, The isoflavone metabolite 6-methoxyequol inhibits angiogenesis and suppresses tumor growth, Mol Cancer. 11 (2012) 35.
[43] Q. Yu, S. Huang, Z. Wu, J. Zheng, X. Chen, L. Nie, Label-free visualization of early cancer hepatic micrometastasis and intraoperative image-guided surgery by photoacoustic imaging, J Nucl Med. 61 (7) (2020) 1079–1085.
[44] Z. Wang, X. Wang, J. Wan, F. Xu, N. Zhao, M. Chen, Optical imaging in the second near infrared window for vascular bioimaging, Small. 17 (2021) 2103780.
[45] Y. Su, B. Yu, S. Wang, H. Cong, Y. Shen, NIR-II bioimaging of small organic molecule, Biomaterials. 271 (2021), 120717.
[46] M. Dougan, J.R. Ingram, H.-J. Jeong, M.M. Mosaheb, P.T. Bruck, L. Ali, N. Pishesha, O. Blomberg, P.M. Tyler, M.M. Servos, M. Rashidian, Q.-D. Nguyen, U.H. von Andrian, H.L. Ploegh, S.K. Dougan, Targeting cytokine therapy to the pancreatic tumor microenvironment using PD-L1 specific VHHs, Cancer Immunol Res. 6 (2018) 389-401.
[47] J. Lv, Y. Liu, F. Cheng, J. Li, Y. Zhou, T. Zhang, N. Zhou, C. Li, Z. Wang, L. Ma, M. Liu, Q. Zhu, X. Liu, K. Tang, J. Ma, H. Zhang, J. Xie, Y. Fang, H. Zhang, N. Wang, Y. Liu, B. Huang, Cell softness regulates tumorigenicity and stemness of cancer cells, EMBO J. 40 (2021) e106123.
[48] R. Chen, S. Huang, T. Lin, H. Ma, W. Shan, F. Duan, J. Lv, J. Zhang, L. Ren, L. Nie, Photoacoustic molecular imaging-escorted adipose photodynamic–browning synergy for fighting obesity with virus-like complexes, Nat. Nanotechnol. 16 (4) (2021) 455–465.
[49] L. Lin, P. Hu, X. Tong, S. Na, R. Cao, X. Yuan, D.C. Garrett, J. Shi, K. Maslov, L. V. Wang, High-speed three-dimensional photoacoustic computed tomography for preclinical research and clinical translation, Nat Commun. 12 (2021) 882.
[50] D.i. Zhang, Z. Wang, L.u. Wang, Z. Wang, H. Wang, G. Li, Z.-Y. Qiao, W. Xu, H. Wang, High-performance identification of human bladder cancer using a signal self-amplifiable photoacoustic nanoprobe, ACS Appl. Mater. Interfaces. 10 (34) (2018) 28331–28339.
[51] S. Naito, F. Algaba, M. Babjuk, R.T. Bryan, Y.-H. Sun, L. Valiquette, J. de la Rosette, The clinical research office of the endourological society (CROES) multicentre randomised trial of narrow band imaging–assisted Transurethral Resection of Bladder Tumour (TURBT) Versus Conventional White Light Imaging-Assisted TURBT in primary non–muscle-invasive bladder cancer patients: trial protocol and 1-year results, European Urology. 70 (2016) 506–515.
[52] H. Gao, Shaping tumor microenvironment for improving nanoparticle delivery, Current Drug Metabolism. 17 (8) (2016) 731–736.
[53] S. Cheng, B. Shen, W. Yuan, X. Zhou, Q. Liu, M. Kong, Y. Shi, P. Yang, W. Feng, F. Li, Time-gated ratiometric detection with the same working wavelength to minimize the interferences from photon attenuation for accurate in vivo detection, ACS Cent. Sci. 5 (2) (2019) 299–307.